

Investigation of coherent structures generated by acoustic tube in turbulent flow separation control

Xingyu Ma · Reinhard Geisler · Janos Agocs ·
Andreas Schröder

Received: 26 September 2014 / Revised: 12 January 2015 / Accepted: 28 January 2015 / Published online: 15 February 2015
© Springer-Verlag Berlin Heidelberg 2015

Abstract An acoustic tube was designed in order to control the turbulent flow separation downstream of a backward-facing step. The Reynolds number based on the free-stream velocity and the step height was $Re_h = 2.0 \times 10^4$. As an active flow control device, the acoustic tube generated periodic pressure perturbations at a frequency of $f_a = 100$ Hz, which was close to the most amplified frequency of the shedding instability of the turbulent shear layer. Spanwise vortices rolled up due to the perturbations. 2D–2C particle image velocimetry was used to measure separated shear layer and the reattachment area downstream of the BFS. The flow control results show that the acoustic tube can suppress recirculation regions behind the step and reduce the reattachment length by 43.7 %. The roll-up and pairing processes of the vortices lead to an increase in the total Reynolds shear stress. The coherent structures are extracted by proper orthogonal decomposition and represented by two pairs of modes, of which the coherence is analyzed by the corresponding coefficients. Both the primary and secondary series of vortices are reconstructed as traveling waves with the fundamental frequency f_a and the overtone frequency $2f_a$, respectively.

1 Introduction

Investigation of coherent structures has been subject of various turbulence studies since the 1960s. The early discoveries came from flow visualization experiments. Low-speed

streaks were first found in near-wall regions of turbulent boundary layers by Kline et al. (1967) using hydrogen bubbles method. The existence of large-scale coherent structures in turbulent mixing layers was verified by Brown and Roshko (1974). As further research was carried out on turbulent mixing layers (Lewalle et al. 2000; Aubrun et al. 2002; Kit et al. 2005), free shear layers (Roos and Kegelmann 1986; Garg and Cattafesta 2001; Brun et al. 2008; Bade and Foss 2010) and turbulent boundary layers (Wark and Nagib 1991; LeHew et al. 2013; Gao et al. 2013), understanding of turbulence has gradually been changed. Being different from the early understanding that turbulence is essentially a stochastic phenomenon having random fluctuating motions superimposed on a well-defined mean flow (Taylor 1935), it has been gradually realized that the transport properties of most turbulent shear flows are dominated by large-scale coherent motions that are not random (Cantwell 1981). A coherent structure was defined as a connected turbulent fluid mass with instantaneously phase-correlated vorticity over its spatial extent (Hussain 1986). Later, the definition was expanded to other fundamental flow variables (velocity component, density and temperature) that exhibited positive auto- or cross-correlation values over a range of space or time (Robinson 1991). Such coherent motions play a predominant role in turbulent shear flows such as boundary layers and separated shear layers. It is believed that ‘The understanding of coherent structures clearly holds the key to understanding turbulence management and control’ (Hussain 1986). The present work focuses on the use of coherent structures in turbulent flow separation control downstream of a backward-facing step.

Turbulent flow over a backward-facing step (BFS) is a multi-scale problem containing a separated shear layer, recirculation regions and reattachment area (Fig. 1).

X. Ma (✉) · R. Geisler · J. Agocs · A. Schröder
Institute of Aerodynamics and Flow Technology, German
Aerospace Center (DLR), Bunsenstrasse 10, 37073 Göttingen,
Germany
e-mail: xingyu.ma@dlr.de

Although the BFS has a simple geometry, the flow separation and reattachment are still complex (Eaton and Johnston 1981). As Reynolds number increases, small- and smaller-scale vortices evolve in addition to large-scale recirculation flow, which makes the flow field even more complex. However, a two-dimensional BFS provides a typical case of flow separation at a fixed separation line. Therefore, BFS has been widely used as a fundamental flow case by many researchers for flow control studies. The primary goal of most flow control studies is to reduce the non-dimensional reattachment length L/h , which is defined as the distance from the step to where the mean flow reattaches on the plate surface. The reduction rate $R = (L_0 - L)/L_0$ is used to measure the flow control effectiveness. Eaton and Johnston (1981) provided an extensive review of the experimental studies on this topic and discussed the effects of various parameters on reattachment length. Initial boundary layer state (laminar or turbulent), ratio of boundary layer thickness to step height, aspect ratio of step width to height and other parameters may influence reattachment length downstream. Armaly et al. (1983) investigated laminar, transitional and turbulent BFS flows in a two-dimensional channel at $70 < Re < 8,000$ by experiments. It was concluded that, if the boundary layer was fully turbulent, the reattachment length lied around $7 < L/h < 8$ and became independent of Reynolds number. Active control devices were applied to reduce reattachment lengths by many researchers. The Strouhal number based on step height $St_h = fh/U_0$ is frequently used as a non-dimensional perturbation

frequency. Bhattacharjee et al. (1986) used a loudspeaker above the BFS to influence the flow and found that the effective forcing was in a range of $St_h = 0.2\text{--}0.4$. Chun and Sung (1996) applied a sinusoidal oscillating jet at the separation edge in a BFS flow at $Re = 23,000$. It was found that an effective perturbation at $St_h = 0.29$ reduced the reattachment length by 35 %. The same effective non-dimensional perturbation frequency $St_h = 0.29$ was also proposed by Roos and Kegelmann (1986) by using an oscillating flap at the step edge. Besides, another important parameter is the Strouhal number based on the momentum thickness of boundary layer $St_\theta = f\theta/U_0$. Hasan (1992) found two distinct modes of instability in laminar separation over a BFS, which were the ‘shear layer mode’ at $St_\theta = 0.012$ and the ‘step mode’ at $St_h = 0.185$. Comparison of the present BFS flow configuration with the literature is listed in Table 1. Although numerous investigations have been carried out on this topic, a complete understanding of the physical mechanism of turbulent shear layer and reattachment has still not been obtained.

Another motivation of studying BFS flow comes from the presence of separated and reattached flows in many engineering applications. This phenomenon usually results in undesired unsteadiness, vibrations and noise. For instance, unsteady vortices shed from an afterbody of a launch vehicle and then hit nozzles behind resulting in unsteady loads and vibrations. Moreover, it also exists in the joint of a high-speed train or the sunroof of a car. Thus, there is great demand of better understanding and proper solutions to the problem not only in scientific research, but also in engineering applications (Stark and Wagner 2009; Lüdeke and Calvo 2011; Statnikov et al. 2013).

There are four parts in the present paper. The first section provides a brief introduction and research background of coherent structures and active flow control research on backward-facing step flows. In the following section, the design of an acoustic tube and PIV measurement are presented. In the third section, the measurement results are analyzed by time- and phase-averaging methods and by POD. The flow control effect and the coherent structures are discussed in detail. The fourth section gives a conclusion of the present work and a brief outlook for future research.

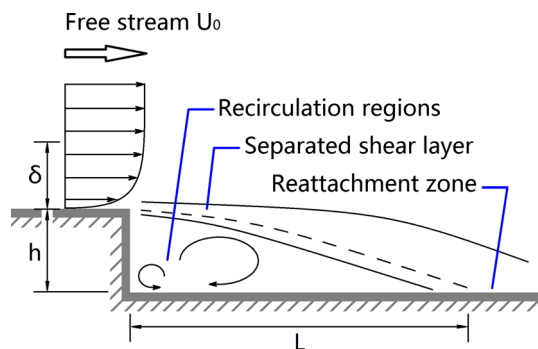


Fig. 1 Sketch of turbulent backward-facing step flow

Table 1 Comparison of the present BFS flow with the literature

References	h (mm)	δ/h	θ/h	Aspect ratio	B. L. state	Re_h	L/h	Note
Roos and Kegelmann (1986)	89	0.38	–	10	Turbulent	20,000	5.5	Wind tunnel
Bhattacharjee et al. (1986)	56	–	0.018	16.25	Turbulent	45,000	6.0	Wind tunnel
Hasan (1992)	30	0.15	0.023	20	Laminar	11,000	–	Wind tunnel
Chun and Sung (1996)	50	0.38	0.036	12.5	Turbulent	23,000	7.20	In a channel with a height of 3 h
Present	30	0.5	0.066	43.3	Turbulent	20,000	7.1	Wind tunnel

2 Experimental apparatus and procedure

2.1 Flow facility

The experiments were carried out in the 1-m wind tunnel at the German Aerospace Center (DLR) in Göttingen, Germany. The open test section had a cross section of $1,050 \times 700 \text{ mm}^2$. The free-stream velocity was $U_0 = 10 \text{ m/s}$ with a turbulence level of 0.15 %. A backward-facing step model was mounted horizontally on a flat plate with an elliptical leading edge. The model was placed in the open test section without side plates or top plate. The BFS was 900 mm long and 1,300 mm wide with a step height of $h = 30 \text{ mm}$. The aspect ratio of width to height was 43.3, which was larger than the two-dimensionality criterion of 10 (de Brederode and Bradshaw 1978) for assuming a two-dimensional average flow in the center portion of the step. The incoming boundary layer was tripped at the leading edge by zigzag bands with a thickness of 0.4 mm to generate a turbulent boundary layer. The thickness of the turbulent boundary layer at the separation was $\delta \approx 15 \text{ mm}$, resulting in a ratio of boundary layer thickness to step height of $\delta/h \approx 0.5$. The Reynolds number, based on the free-stream velocity $U_0 = 10 \text{ m/s}$ and the step height $h = 30 \text{ mm}$, was $Re_h = 2.0 \times 10^4$. A two-dimensional coordinate system has its origin point at the corner on the wall, a streamwise X-axis and a vertical Y-axis.

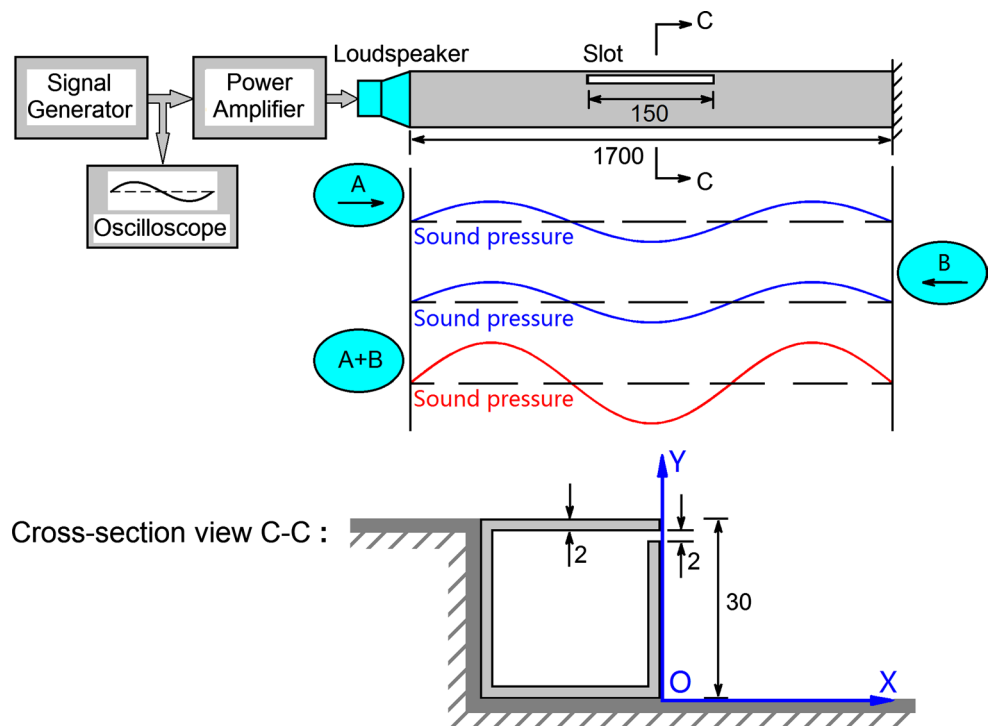
2.2 Acoustic tube

An acoustic tube has been designed and integrated with the BFS in order to control the flow separation downstream. The acoustic tube consists of a spanwise tube of $l = 1.7 \text{ m}$ length with a square cross section of $30 \times 30 \text{ mm}^2$. A thin slot of $150 \times 2 \text{ mm}^2$ was near the separation edge with its exit in the flow direction (Fig. 2). The acoustic tube is equipped with a loudspeaker (max. 100 W, 8 Ω) installed on one side, while the other side is sealed by a hard surface. When single-frequency sound waves propagate along the tube, interference occurs between the incident and reflected sound waves. If the half wavelength fits the length of the tube, standing waves are created. The air inside the tube is compressed like a spring. In the center part of the acoustic tube, the antinode of the standing wave has the maximum pressure fluctuation, which perturbs the shear layer at a certain frequency. Although the standing wave had a spanwise distribution, the length of the slot is only 8.8 % of the half wavelength. So the perturbation at the slot can be considered to be approximately uniform. The perturbation frequencies are:

$$f_a = n \times \frac{c}{2 \times l}, \quad n = 1, 3, 5, 7, 9 \quad (1)$$

$c = 340 \text{ m/s}$ is the speed of sound and $l = 1.7 \text{ m}$ is the length of the acoustic tube. The control signals of sine

Fig. 2 Sketch of acoustic tube integrated with backward-facing step. *Sinusoidal lines* indicate sound pressures of sound waves



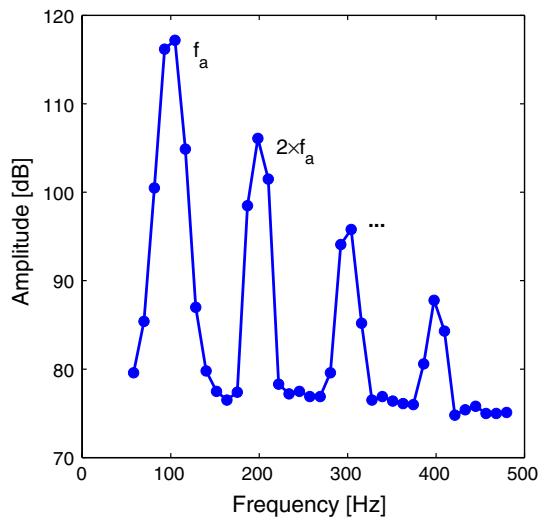


Fig. 3 Frequency spectrum of the acoustic perturbation at $f_a = 100$ Hz and SPL = 110 dB

waves are generated by an Agilent waveform generator and then amplified by a Dynacord CL1600 power amplifier. When the perturbation frequency was $f_a = 100$ Hz, outward acoustic perturbations at the exit of the slot were measured by a mobile NTI microphone for acoustic calibration. The frequency spectrum indicates that the output perturbations contain the fundamental frequency f_a as well as the overtones with higher frequencies (Fig. 3). In the parameter study, five perturbation frequencies $f_a = 100, 300, 500, 700$ and 900 Hz and three sound pressure levels SPL = 105, 110 and 115 dB at the exit of the slot were tested in order to find the parameter influences on the reattachment length.

2.3 2D–2C PIV measurements

Digital PIV systems have been widely used in fluid measurements for about two decades (Raffel et al. 2007). With the development of high-resolution cameras, the 2D–2C PIV technique has been able to capture a large range of scales in fluid motions. Nowadays, it is possible to measure the turbulent boundary layer, separated shear layers and reattachment area in the BFS flow in a single field of view (FOV). In the present measurement, the flow was illuminated by a horizontal–vertical laser light sheet with a thickness of 1 mm from downstream orientation (Fig. 4). The two laser pulses, generated by a Big Sky Ultra CFR Nd:YAG laser system, delivered an energy of 30 mJ per pulse and had 150 μ s time delay. The flow was homogeneously seeded by DEHS droplets with a mean diameter of 1 μ m (Raffel et al. 2007). Particle images were recorded by a high-resolution camera PCO 4000 with a Nikon lens (85 mm, $f/4$) mounted outside the flow field with its optical axis perpendicular to the laser light sheet. Each image

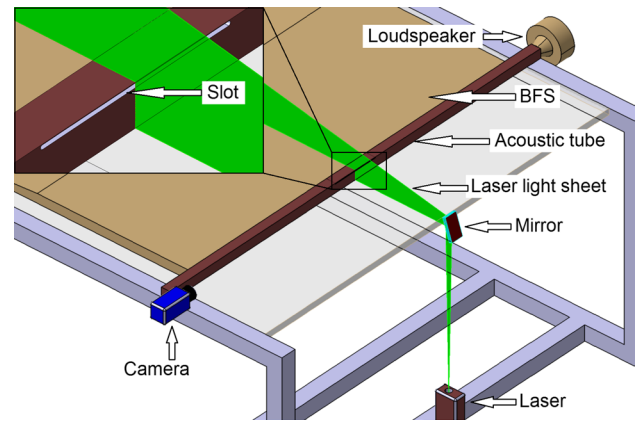


Fig. 4 Sketch of the PIV setup and close-up view of the slot

consisted of an array size of $3,900 \times 910$ pixels covering a measurement area of 310×70 mm² in X- and Y-directions, respectively. A constant magnification factor between the image and physical coordinates was obtained by a PIV calibration process. Synchronization of the image recordings and laser pulses was accomplished by TTL signals from a programmable sequencer. In the first step, 4,000 statistically independent double-frame images were recorded for the flows with and without perturbation in order to calculate time averages and corresponding root-mean-square values of the velocity vector fields. In the second step, 1,000 phase-locked double-frame images at 12 phases in one period were recorded in order to capture periodic motions in the turbulent shear layer. Image evaluation was performed using PIVview software from PIVTEC. As a preprocess procedure, a minimum background image was subtracted from the particle images in order to reduce noise and eliminate local light inhomogeneity. Then, the double-frame images were evaluated by a multi-grid cross-correlation method (Willert and Gharib 1991) with image deformation and a final interrogation window size of 16×16 pixel at 75 % overlap, resulting in a vector spacing of 0.3 mm (0.01 h) in the physical coordinate.

3 Measurement results and analysis

3.1 Parameter study and flow control result

In the parameter study, the main parameters include the non-dimensional perturbation frequency $St_h = f_a h/U_0$ and the sound pressure level (SPL). These two parameters have different influences on the flow control effect. Phase-averaged vortical structures at different frequencies and the same SPL are compared in Fig. 5 to show the frequency response of the turbulent shear layer. If the perturbation frequency is at $St_h = 0.3$ ($f_a = 100$ Hz), which is close to

the most amplified frequency of the turbulent shear layer (Ma et al. 2014b), apparent spanwise vortices are generated due to the periodic perturbation. The reattachment length is $L/h = 4.0$. The corresponding Strouhal number based on the momentum thickness is $St_\theta = 0.02$, which is a little higher than the ‘shear layer mode’ at $St_\theta \approx 0.012$ for laminar separations (Hasan 1992). Table 2 shows the comparison of non-dimensional frequencies and reattachment lengths in the present experiment and the literature. If the frequency increases to $St_h = 0.9$, the periodic vortices become much smaller and decay quickly downstream. The reattachment length increases to $L/h = 6.5$. For even higher frequencies $St_h \geq 1.5$, the periodic vortices are

hardly detected and the reattachment length increases to $L/h = 7.3$. This agrees well with the experimental results reported by Chun and Sung (1996) that the effective perturbation was at $St_h = 0.29$ and higher frequencies above $St_h \geq 1.0$ may increase the reattachment length. On the other hand, phase-averaged vortical structures at the same frequency and different SPLs are compared in Fig. 6 to show the amplitude response of the turbulent shear layer. The respective reattachment lengths are $L/h = 4.3, 4.0, 4.0$. As the SPL increases, the vortical structures have increasing scales and similar formations, but the reattachment length remains almost the same. Therefore, based on the reduction of the reattachment length among the tested

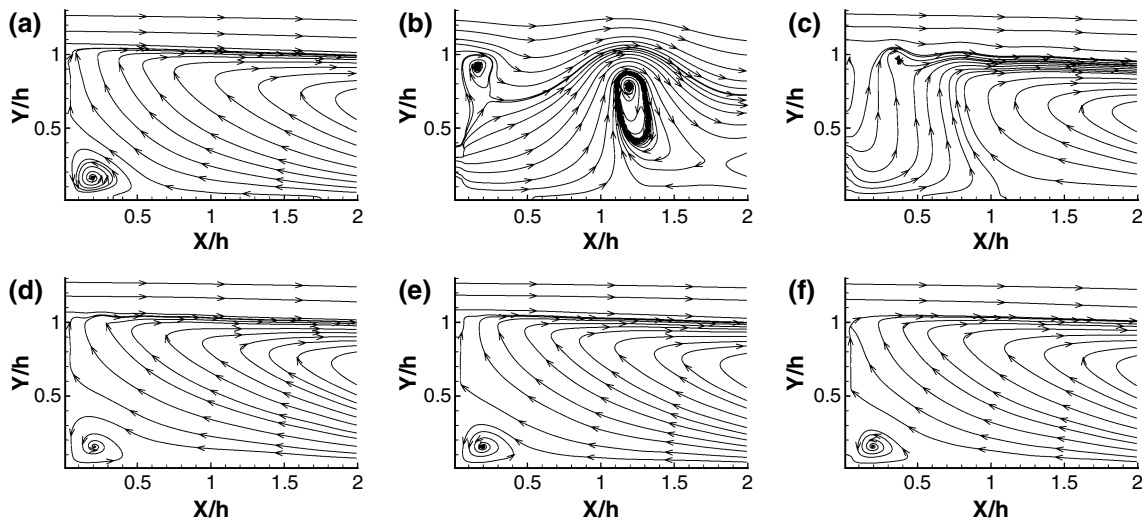


Fig. 5 Phase-averaged streamlines at the same SPL = 110 dB and different frequencies. **a–f** $St_h = 0, 0.3, 0.9, 1.5, 2.1$ and 2.7

Table 2 Reduction of reattachment lengths in the present experiment and the literature

References	Control method	St_h	St_θ	L_0/h	L/h	R (%)
Roos and Kegelmann (1986)	Oscillating flap	0.29	–	5.5	4.5	18.2
Bhattacharjee et al. (1986)	Acoustic perturbation	0.28	0.005	6.0	5.0	16.7
Hasan (1992)	Acoustic perturbation	0.14–0.85	0.003–0.02	–	–	–
Chun and Sung (1996)	Acoustic perturbation	0.29	0.01	7.2	4.68	35.0
Present	Acoustic perturbation	0.3	0.02	7.1	4.0	43.7

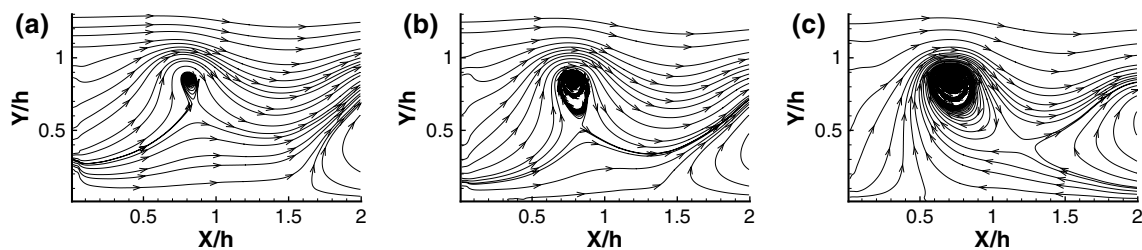
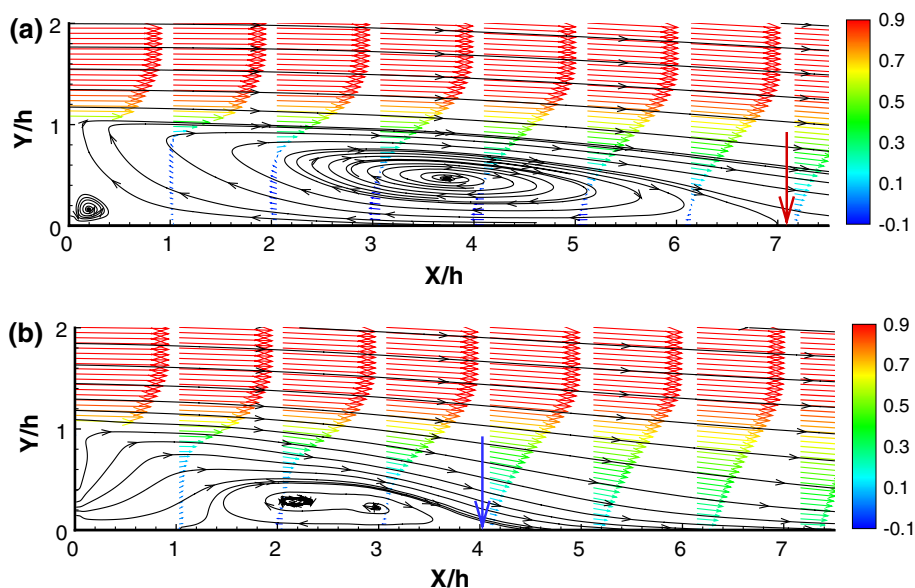


Fig. 6 Phase-averaged streamlines at the same frequency $St_h = 0.3$ and different SPLs. **a–c** SPL = 105, 110 and 115 dB

Fig. 7 Time-averaged velocity vector fields of the clean (a) and controlled (b) cases. The *arrows* indicate the reattachment lengths. The *color* indicates the streamwise velocity component \bar{u}/U_0



parameter sets, the case at $St_h = 0.3$ and $SPL = 110$ dB is selected as a ‘controlled case’ for further analysis.

Time-averaged velocity vector fields of the clean and controlled cases are shown in Fig. 7. In the clean case, the main and the secondary recirculation regions are identified behind the step and the reattachment length is $L_0/h = 7.1$. In the controlled case, the non-dimensional frequency is $St_h = 0.3$ and the ratio of the root-mean-square of the fluctuating velocity magnitude to free-stream velocity is $|U|_{rms}/U_0 = 0.18$. The comparison shows that the streamlines are drawn downward closer to the wall. The main recirculation region is clearly suppressed, and its center position moves upstream and closer to the wall from the point $(X/h = 3.74, Y/h = 0.47)$ to $(X/h = 2.57, Y/h = 0.30)$. The reattachment length is reduced to $L/h = 4.0$, resulting in a reduction rate of $R = 43.7\%$. It is noted in Fig. 7b that the secondary recirculation region disappears and the time-averaged streamlines start from the step wall. One reason for the three-dimensional spanwise mean flow is that the spanwise limited acoustic perturbations could entrain neighboring fluid into the low-pressure low-speed recirculation region. As a result, the recirculation region is smaller than that of the clean case. The other reason is the asymmetric design of the acoustic tube. It had one loudspeaker as sound source mounted on one side and was sealed by a hard plate on the other side. In that way, the acoustic perturbation along the slot is asymmetric: It is found that the SPL along the slot shows quit small differences (a few dB), compared with the $SPL = 110$ dB at the center of the slot.

3.2 Phase-averaged flow fields

The phase-locked measurements provide insight into the development of the coherent structures related to the

periodic perturbation in the turbulent shear layer. By applying the triple decomposition (Hussain and Reynolds 1970), the velocity vector can be decomposed as:

$$u = \bar{u} + \tilde{u} + u' \tag{2}$$

The left term is the instantaneous velocity vector. The right terms are the mean, periodic and random fluctuating parts, which correspond to time-averaged flow, coherent structures and incoherent turbulence, respectively. Then, the phase-averaged velocity is obtained as:

$$\langle u \rangle = \bar{u} + \tilde{u} = u - u' \tag{3}$$

The phase-averaged velocity vector fields are shown in Fig. 8. Spanwise vortices roll up, approximately within $0 < X/h < 1.5$, at the beginning of the shear layer. The distance between the first two vortices is approximately $\Delta X/h \approx 1.0$. Further downstream approximately within $1.5 < X/h < 4$, the vortices with a growing size move downstream toward the wall and vortex pairing occurs near the wall. The distance between the vortices increases to $\Delta X/h \approx 1.5$. The phase-averaged streamlines of the outer flow are drawn closer to the wall.

3.3 Reynolds shear stress

Reynolds shear stress is an important quantity of momentum transfer in turbulent flows. It represents the quantity of the fluid particles fluctuating upward and downward between the shear layers (Schlichting 1979). Based on the triple decomposition, the Reynolds shear stress can be decomposed as:

$$\tau'_{xy} = -\rho \cdot \overline{(\tilde{u} + u') \cdot (\tilde{v} + v')} \tag{4}$$

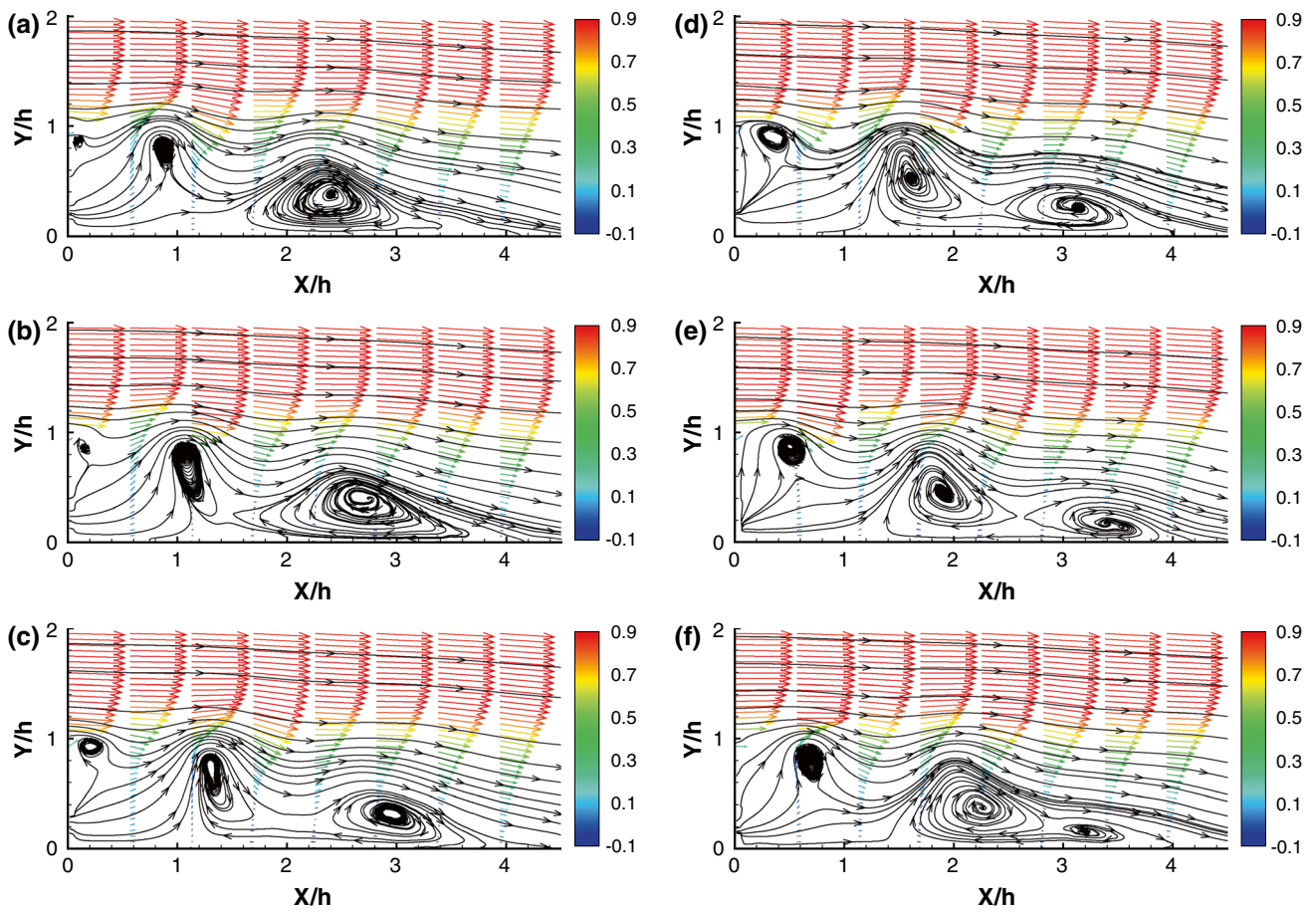


Fig. 8 Phase-averaged flow vector fields of the controlled case. (a)–(f): 0°, 60°, 120°, 180°, 240° and 300°. The *color* indicates the streamwise velocity component $\langle u \rangle / U_0$

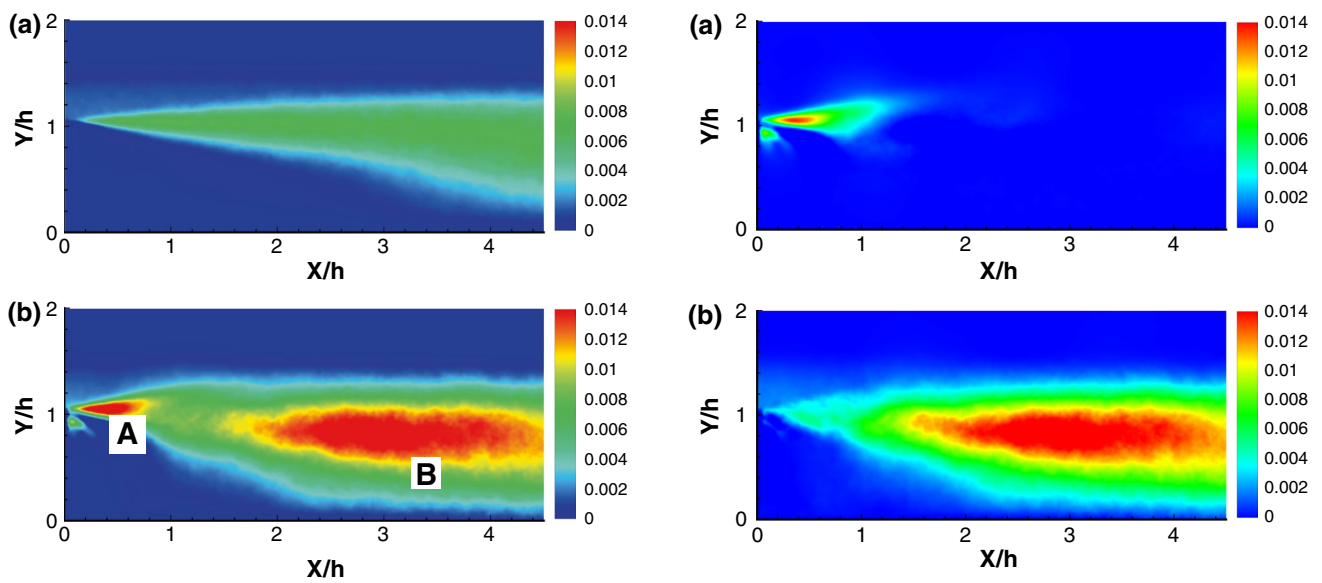


Fig. 9 Total Reynolds shear stress $-\left(\overline{\tilde{u} \cdot \tilde{v}} + \overline{u' \cdot v'}\right) / U_0^2$. **a** Clean case and **b** controlled case

Fig. 10 Decomposition of Reynolds shear stress of the controlled case. **a** Coherent part $-\overline{\tilde{u} \cdot \tilde{v}} / U_0^2$ and **b** incoherent part $-\overline{u' \cdot v'} / U_0^2$

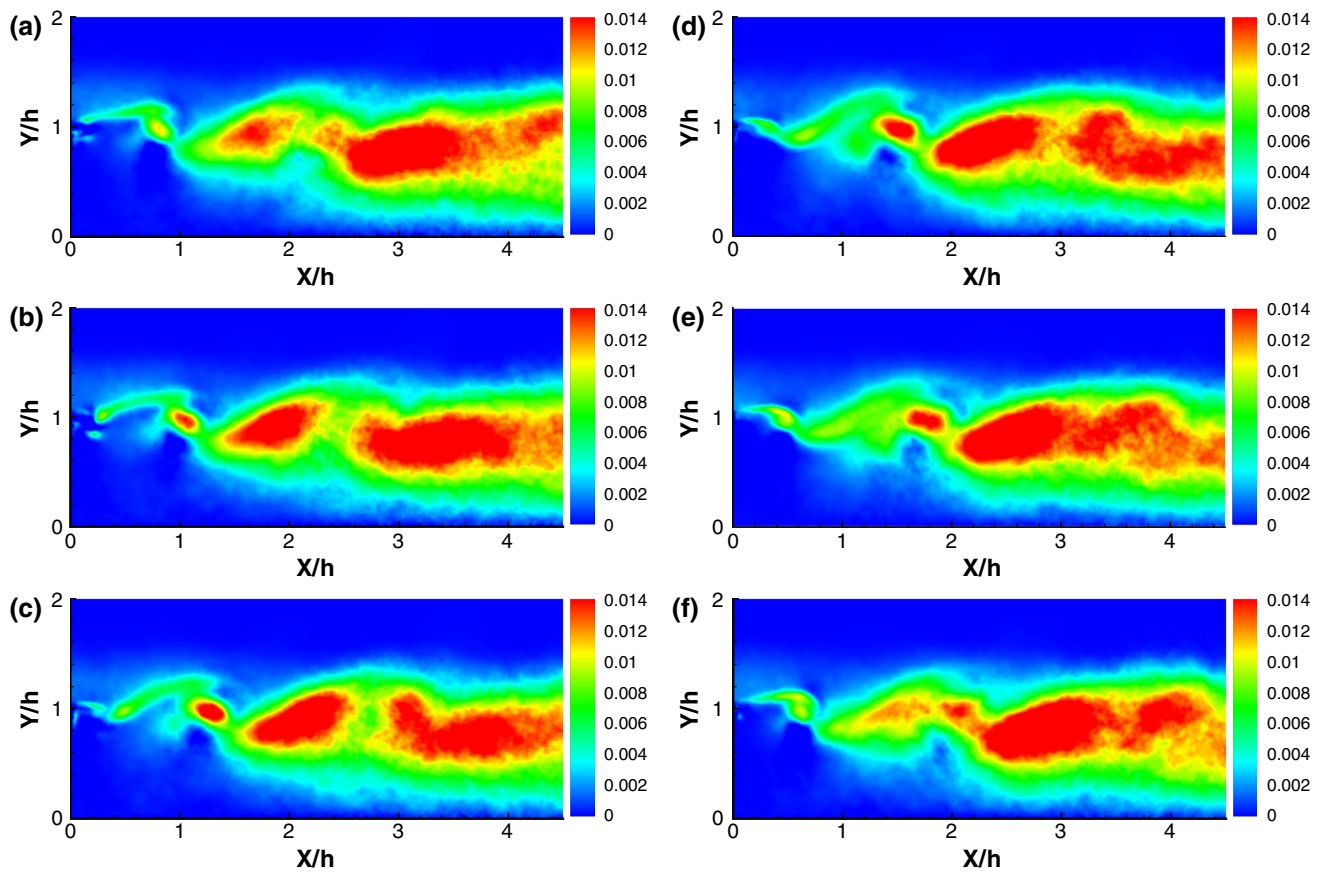


Fig. 11 Phase-averaged incoherent Reynolds shear stresses $-\langle u' \cdot v' \rangle / U_0^2$ of the controlled case. **a–f** $0^\circ, 60^\circ, 120^\circ, 180^\circ, 240^\circ$ and 300°

Additionally, the periodic components are uncorrelated with the random fluctuations:

$$\overline{\tilde{u} \cdot v'} = 0, \overline{u' \cdot \tilde{v}} = 0 \tag{5}$$

So the Reynolds shear stress is decomposed as:

$$\tau'_{xy} = -\rho \cdot \left(\overline{\tilde{u} \cdot \tilde{v}} + \overline{u' \cdot v'} \right) \tag{6}$$

On the right-hand side, the first part $\overline{\tilde{u} \cdot \tilde{v}}$ is the contribution of the coherent structures and the second part $\overline{u' \cdot v'}$ is the contribution of the incoherent turbulence.

The comparison in Fig. 9 shows that the total Reynolds shear stress is increased by the periodic perturbations and there are two distinct high-value regions A and B in the controlled case. The contributions of the coherent and incoherent motions are compared in Fig. 10 (Ma et al. 2014a). The spanwise vortices roll up near the acoustic tube at approximately $X/h \approx 0.5$ and contribute the major part of the high Reynolds shear stress in the region A. On the other hand, incoherent turbulence contributes Reynolds shear stress in the entire shear layer and the vortex pairing and breakdown result in higher Reynolds shear stress in the region B. Therefore, the coherent structure plays an

important role in the transports of mass and momentum in ‘its own territory’ (Hussain 1986) and makes the comparable contribution as the incoherent turbulence.

Figure 11 shows the incoherent Reynolds shear stresses that are obtained from the phase-locked flow fields. The interface between the shear layer and the outer flow is evolving with the movements of the spanwise vortices. It is clear that the vortex roll-up and breakdown play predominant roles in the shear layer and both processes are related to the increase in Reynolds shear stress. The high momentum fluid mass is entrained due to the Biot–Savart induction and then is engulfed into the turbulent shear layer (Hussain 1986). This entrainment produces more turbulent motions in the shear layer than turbulent mixing process due to viscosity alone, which results in more spread of the shear layer and reduction of the reattachment length.

3.4 POD Analysis

POD is an effective method for identifying coherent structures in the flow by linear decomposition and reconstruction (Lumley 1967). In order to reveal the spatial structures of the vortices, the snapshot POD method (Sirovich

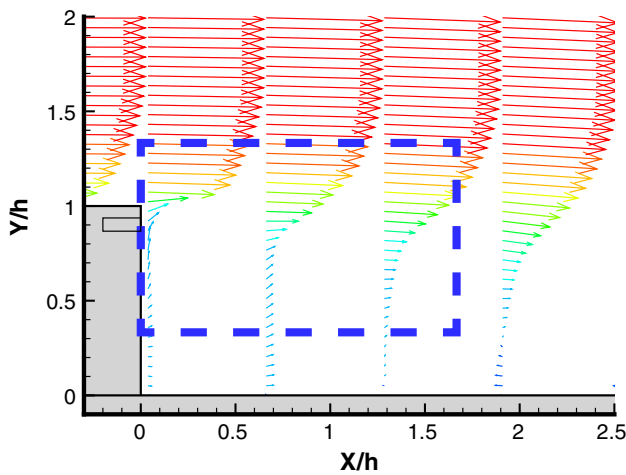


Fig. 12 Sketch of the rectangular region where POD is applied

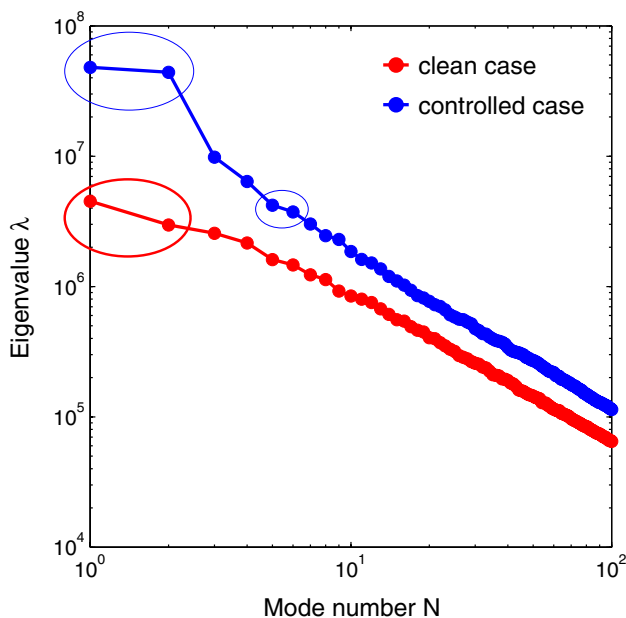


Fig. 13 POD eigenvalue distributions of the first 100 modes

1987) is applied in a rectangular region (Fig. 12) which has a size of $1.7 h \times 1 h$. Detailed mathematical algorithm of the snapshot POD method is presented by Meyer et al. (2007). This method decomposes the original velocity data sequence into the mean flow and the linear combination of spatial orthogonal modes as:

$$U = \bar{U} + \sum_{i=1}^N a_i \cdot \Phi_i \tag{7}$$

Φ_i is the i th mode and a_i is the corresponding coefficient. All the modes are ranked decreasingly based on the eigenvalues, which represent the turbulent kinetic energy

(Meyer et al. 2007). This energy-based hierarchy ensures that predominant and large-scale flow structures can be represented by the first few modes. In the present analysis, the number of the instantaneous velocity vector fields that are used is $N = 4,000$ and each snapshot contains 15,974 spatial points.

The POD eigenvalue distributions of the clean and controlled cases are plotted in Fig. 13. For both cases, the first two modes contain the most turbulent kinetic energy and the other modes decay exponentially. The comparison shows that the energetic fluctuating motions of the controlled case are greater than those of the clean case. Additionally, the first two modes of the controlled case contain nearly equivalent energy. By scattering the coefficients of two modes, the coherent interrelations can be revealed. Three typical pairs of modes are depicted by the ellipses in Fig. 13, which are POD_1 and POD_2 of the clean case, POD_1 and POD_2 of the controlled case and POD_5 and POD_6 of the controlled case. Two geometrical variables of a scatter point (a_i, a_j) , phase angle φ (Perrin et al. 2007) and radius r , are defined as

$$\varphi = \arctan \left(\frac{\sqrt{\lambda_i}}{\sqrt{\lambda_j}} \cdot \frac{a_j}{a_i} \right) \tag{8}$$

$$r = \sqrt{a_i^2 + a_j^2} \tag{9}$$

The coefficients of the three pairs of modes are scattered in Fig. 14. In the clean case, the coefficients a_1 and a_2 gather to the center as a disk, which indicates that the two modes are independent and incoherent of each other with respect to a phase relation. In the controlled case, by contrast, the coefficients a_1 and a_2 are organized as a circle, which shows that the two modes are coherent and contain a fixed phase difference. Similar scatter distribution is also found for the coefficients a_5 and a_6 of the controlled case. The other modes of the controlled case do not contain this coherent feature.

In order to describe the radial distributions quantitatively, relative standard deviation (RSD) is used to measure how the coefficient points are scattered near the circle of the mean radius:

$$RSD = \frac{\sigma_r}{\bar{r}} \times 100 \% \tag{10}$$

σ_r is the standard deviation of the radius r and \bar{r} is the mean value. Thus, the RSDs of the three cases are 51.9 %, 14.7 % and 37.1 %, respectively. The low value of 14.7 % for POD_1 and POD_2 of the controlled case indicates that most of the points are close to the circle with the mean radius. The high value of 51.9 % for POD_1 and POD_2 of the clean case indicates that all points vary far from the circle.

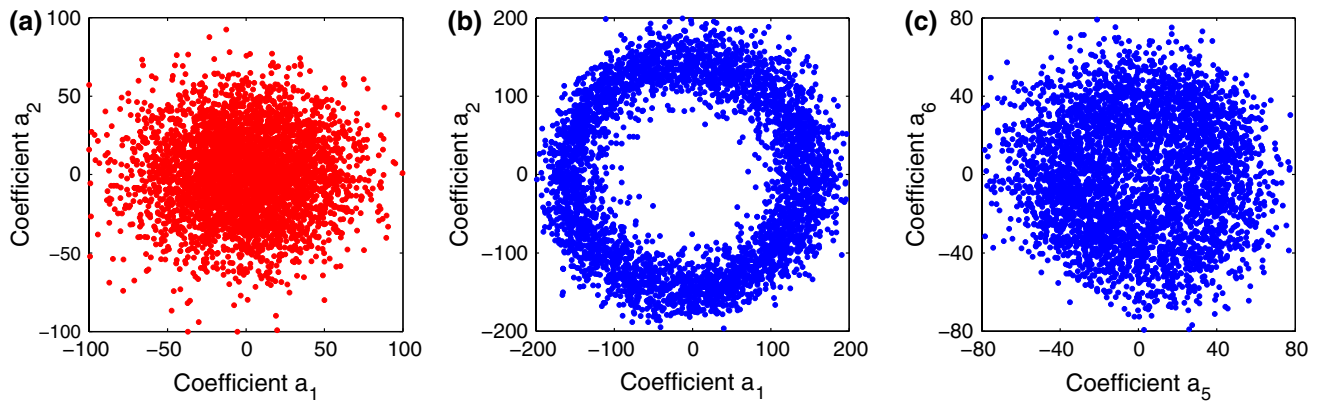


Fig. 14 Scatter distributions of coefficients. **a** POD_1 and POD_2 of the clean case, **b** POD_1 and POD_2 of the controlled case and **c** POD_5 and POD_6 of the controlled case

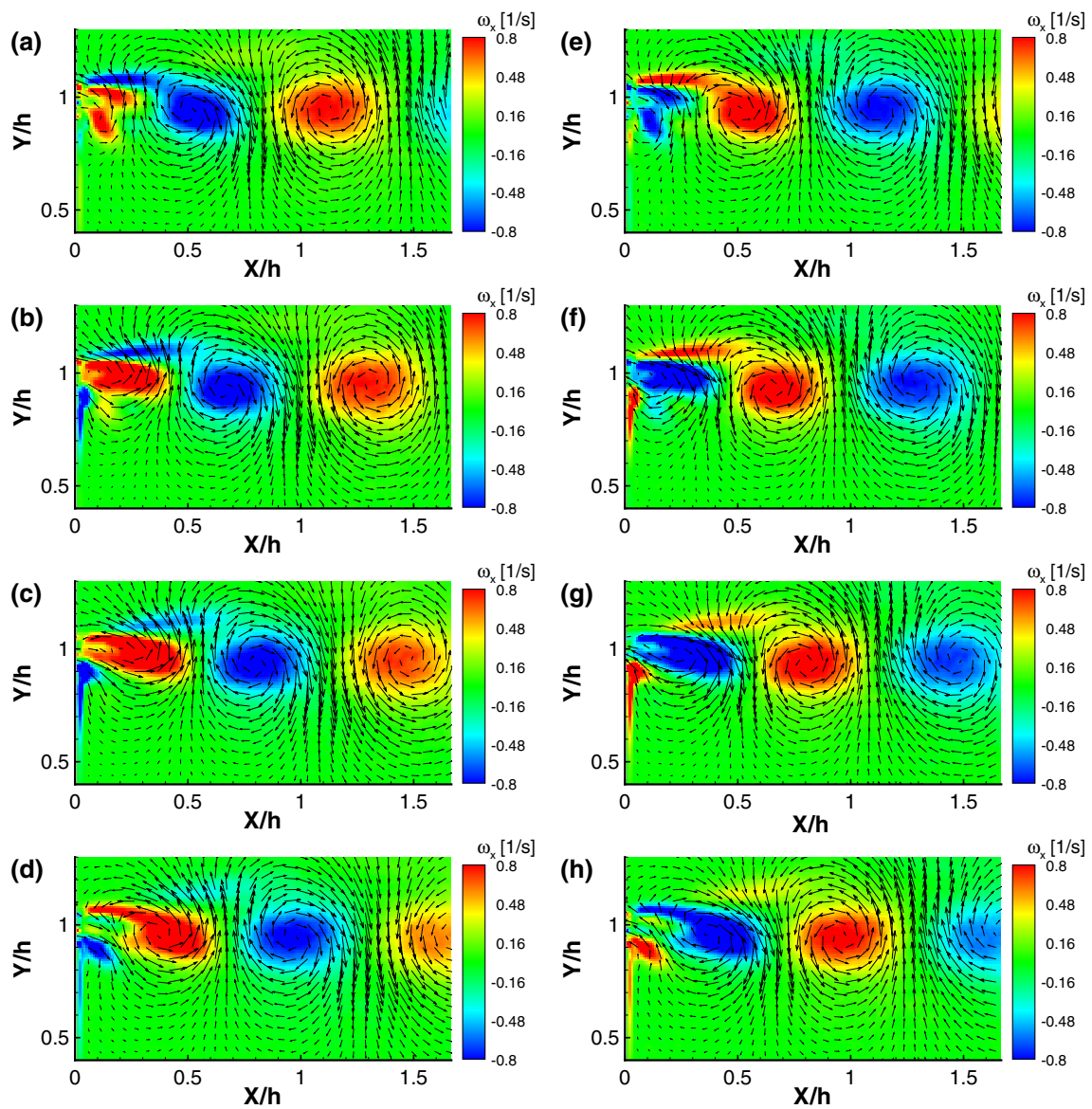


Fig. 15 Reconstructed by $POD_1 + i \cdot POD_2$ of the controlled case. **a–h** $0^\circ, 45^\circ, 90^\circ, 135^\circ, 180^\circ, 225^\circ, 270^\circ$ and 315° . The *color* indicates the spanwise vorticity

POD reconstruction can be obtained by linearly combining modes weighted by corresponding coefficients. As shown in Fig. 15, counter-rotating vortices at different phases are shown in the reconstruction by POD_1 and POD_2 of the controlled case. This regular pattern is a sign of the coherent structures represented by POD_1 and POD_2 which are mutually orthogonal and can be written as a composite form ' $POD_1 + i \cdot POD_2$ ' (Schmid et al. 2012). In other words, the reconstructions are equivalent to the interference of two oscillating modes. An estimated wavelength of the vortices is $\Delta X/h \approx 1.0$, which agrees well with the spatial

scale in the phase-averaged velocity vector fields in Fig. 8. Moreover, the reconstructions by POD_5 and POD_6 of the controlled case show the harmonic counter-rotating vortices with half the wavelength due to the overtone of the acoustic tube (Fig. 16). The phase relation between $\varphi_{1,2}$ and $\varphi_{5,6}$ in Fig. 17 is plotted as a regular pattern other than a uniform distribution, which indicates that the secondary vortices ' $POD_5 + i \cdot POD_6$ ' have doubled frequency of the primary vortices ' $POD_1 + i \cdot POD_2$ '. These vortices show the distinct frequencies and coherent features, which is totally different from the wide frequency bandwidth and

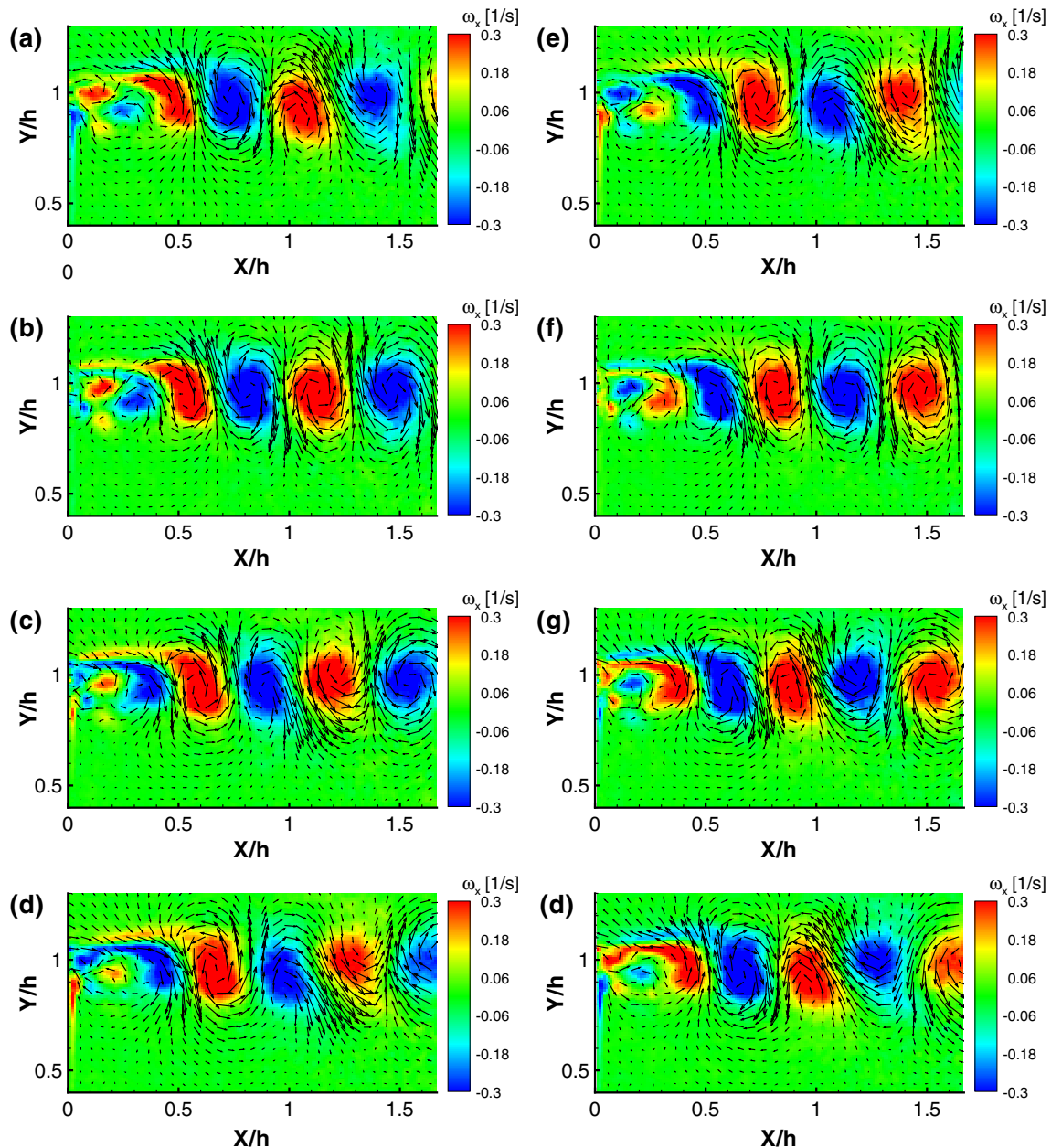


Fig. 16 Reconstructed by $POD_5 + i \cdot POD_6$ of the controlled case. **a–h** $0^\circ, 45^\circ, 90^\circ, 135^\circ, 180^\circ, 225^\circ, 270^\circ$ and 315° . The *color* indicates the spanwise vorticity

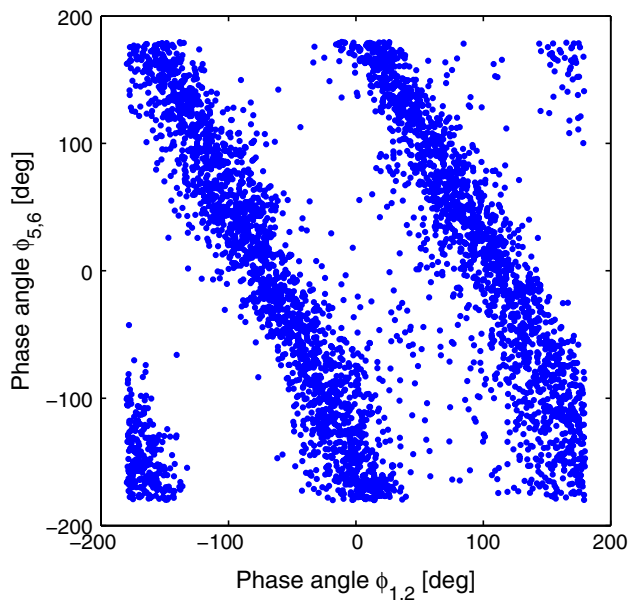


Fig. 17 Phase angle relation between primary and secondary vortices

multi-scale structures as the nature behavior of the clean BFS flow (Bhattacharjee et al. 1986). Thus, it can be concluded that the primary and secondary series of vortices correspond to the fundamental frequency and the overtone of the periodic perturbations.

4 Conclusions

The acoustic tube has been designed and applied in turbulent backward-facing step (BFS) flow. Periodic perturbations can generate spanwise vortices in the turbulent shear layer. Phase-averaged flow fields provide insight into the roll-up and pairing processes. It is revealed that the entrainment is more effective in momentum transfer than turbulent mixing due to viscosity alone. The coherent structures are extracted by POD and represented by pairs of POD modes. The primary and the secondary series of vortices correspond to the fundamental frequency and the overtone of the acoustic tube. Although the standard 2D–2C PIV can achieve velocity information at a high spatial resolution, time information is missing. In future research, time-resolved measurements may be complemented to analyze frequency spectra of the turbulent shear layer and temporal features of the coherent structures.

Acknowledgments The authors would like to thank the German Aerospace Center for supporting the research. The authors gratefully acknowledge valuable discussions with the colleagues at DLR. We are also grateful to Dr. Judith Kokavecz for providing a mobile microphone and valuable suggestions for the acoustic calibration.

References

- Armaly BF, Durst F, Pereira JCF, Schönung B (1983) Experimental and theoretical investigation of backward-facing step flow. *J Fluid Mech* 127:473–496
- Aubrun S, Boisson HC, Bonnet JP (2002) Further characterization of large-scale coherent structure signatures in a turbulent-plane mixing layer. *Exp Fluids* 32:136–142
- Bade KM, Foss JF (2010) Attributes of the large-scale coherent motions in a shear layer. *Exp Fluids* 49:225–239
- Bhattacharjee S, Scheelke B, Troutt TR (1986) Modification of vortex interactions in a reattaching separated flow. *AIAA J* 24(4):623–629
- Brown GL, Roshko A (1974) On density effects and large structure in turbulent mixing layers. *J Fluid Mech* 64:775–816
- Brun C, Aubrun S, Goossens T, Ravier Ph (2008) Coherent structures and their frequency signature in the separated shear layer on the sides of a square cylinder. *Flow Turbul Combust* 81:97–114
- Cantwell BJ (1981) Organized motion in turbulent flow. *Annu Rev Fluid Mech* 13:457–515
- Chun KB, Sung HJ (1996) Control of turbulent separated flow over a backward-facing step by local forcing. *Exp Fluids* 21:417–426
- de Brederode V, Bradshaw P (1978) Influence of the side walls on the turbulent center-plane boundary layer in a square duct. *J Fluid Eng* 100:91–96
- Eaton JK, Johnston JP (1981) A review of research on subsonic turbulent-flow reattachment. *AIAA J* 19:1093–1100
- Gao Q, Ortiz-Duenas C, Longmire EK (2013) Evolution of coherent structures in turbulent boundary layers based on moving tomographic PIV. *Exp Fluids* 54:1625
- Garg S, Cattafesta LN (2001) Quantitative schlieren measurements of coherent structures in a cavity shear layer. *Exp Fluids* 30:123–134
- Hasan MAZ (1992) The flow over a backward-facing step under controlled perturbation: laminar separation. *J Fluid Mech* 238:73–96
- Hussain F (1986) Coherent structures and turbulence. *J Fluid Mech* 173:303–356
- Hussain F, Reynolds WC (1970) The mechanics of an organized wave in turbulent shear layer. *J Fluid Mech* 41:241–258
- Kit E, Krivososova O, Zhilenko D, Friedman D (2005) Reconstruction of large coherent structures from SPIV measurements in a forced turbulent mixing layer. *Exp Fluids* 39:761–770
- Kline SJ, Reynolds WC, Schraub FA, Runstadler PW (1967) The structure of turbulent boundary layers. *J Fluid Mech* 30:741–773
- LeHew JA, Guala M, McKeon BJ (2013) Time-resolved measurements of coherent structures in the turbulent boundary layer. *Exp Fluids* 54:1508–1523
- Lewalle J, Delville J, Bonnet JP (2000) Decomposition of mixing layer turbulence into coherent structures and background fluctuations. *Flow Turbul Combust* 64:301–328
- Lüdeke H, Calvo JB (2011) A fluid structure coupling of the Ariane-5 nozzle section during start phase by detached eddy simulation. *Ceas Space J* 1:33–44
- Lumley JL (1967) The structure of inhomogeneous turbulent flow. *Atmos Turbul Radio Wave Propagation, Moscow*, pp 166–178
- Ma X, Geisler R, Agocs J, Schröder A (2014a) Investigation of coherent structures in active flow control over a backward-facing step by PIV. In: *Proceeding of the 16th International Symposium on Flow Visualization, Okinawa, Japan, 24–27 June 2014*
- Ma X, Geisler R, Agocs J, Schröder A (2014b) Time-resolved tomographic PIV investigation of turbulent flow control by vortex generators on a backward-facing step. In: *Proceeding of the 17th International Symposium on Applications of Laser Techniques to Fluid Mechanics, Lisbon, Portugal, 07–10 July 2014*

- Meyer KE, Pedersen JM, Özcan O (2007) A turbulent jet in crossflow analysed with proper orthogonal decomposition. *J Fluid Mech* 583:199–227
- Perrin R, Braza M, Cid E, Cazin S, Barthet A, Sevrain A, Mockett C, Thiele F (2007) Obtaining phase averaged turbulence properties in the near wake of a circular cylinder at high Reynolds number using POD. *Exp Fluids* 43:341–355
- Raffel M, Willert CE, Wereley ST, Kompenhans J (2007) Introduction. *Particle image velocimetry: A practical guide*, 2nd edn. Springer, Berlin, pp 1–13
- Robinson SK (1991) Coherent motions in the turbulent boundary layer. *Annu Rev Fluid Mech* 23:601–639
- Roos FW, Kegelmann JT (1986) Control of coherent structures in reattaching laminar and turbulent shear layers. *AIAA J* 24:1956–1963
- Schlichting H (1979) *Fundamentals of turbulent flow. Boundary-layer theory*, 7th edn. McGRAW-HILL, New York, pp 555–574
- Schmid PJ, Violato D, Scarano F (2012) Decomposition of time-resolved tomographic PIV. *Exp Fluids* 52:1567–1579
- Sirovich L (1987) Turbulence and the dynamics of coherent structures. Part 1: coherent structure. *Q Appl Math* 45(3):561–571
- Stark R, Wagner B (2009) Experimental study of boundary layer separation in truncated ideal contour nozzles. *Shock Waves* 19:185–191
- Statnikov V, Meiß JH, Meinke M, Schröder W (2013) Investigation of the turbulent wake flow of generic launcher configurations via a zonal RANS/LES method. *Ceas Space J* 5:75–86
- Taylor GI (1935) Statistical theory of turbulence Part 1–4. *Proc R Soc Lond A* 151:421–478
- Wark CE, Nagib HM (1991) Experimental investigation of coherent structures in turbulent boundary layer. *J Fluid Mech* 230:193–208
- Willert CE, Gharib M (1991) Digital particle image velocimetry. *Exp Fluids* 10:181–193